

Structural periodicity in laser additive manufactured Zr-based bulk metallic glass

Cite as: Appl. Phys. Lett. **115**, 031902 (2019); <https://doi.org/10.1063/1.5100050>

Submitted: 14 April 2019 . Accepted: 23 June 2019 . Published Online: 16 July 2019

James P. Best , Zach Evenson, Fan Yang, Ann-Christin Dippel, Moritz Stolpe, Olof Gutowski, M. Tarik Hasib, Xiaopeng Li, and Jamie J. Kruzic 



View Online



Export Citation



CrossMark

ARTICLES YOU MAY BE INTERESTED IN

[Formation of controllable 1D and 2D periodic surface structures on cobalt by femtosecond double pulse laser irradiation](#)

Applied Physics Letters **115**, 031601 (2019); <https://doi.org/10.1063/1.5103216>

[Aberration-corrected cryogenic objective mirror with a 0.93 numerical aperture](#)

Applied Physics Letters **115**, 033701 (2019); <https://doi.org/10.1063/1.5110546>

[Antenna-coupled spintronic terahertz emitters driven by a 1550 nm femtosecond laser oscillator](#)

Applied Physics Letters **115**, 022405 (2019); <https://doi.org/10.1063/1.5089421>

Applied Physics Letters

Mid-IR and THz frequency combs
special collection

[Read Now!](#)



Structural periodicity in laser additive manufactured Zr-based bulk metallic glass

Cite as: Appl. Phys. Lett. **115**, 031902 (2019); doi: [10.1063/1.5100050](https://doi.org/10.1063/1.5100050)

Submitted: 14 April 2019 · Accepted: 23 June 2019 ·

Published Online: 16 July 2019



View Online



Export Citation



CrossMark

James P. Best,¹  Zach Evenson,^{2,a)} Fan Yang,³ Ann-Christin Dippel,⁴ Moritz Stolpe,⁵ Olof Gutowski,⁴ M. Tarik Hasib,¹ Xiaopeng Li,¹ and Jamie J. Kruzic^{1,b)} 

AFFILIATIONS

¹School of Mechanical and Manufacturing Engineering, UNSW Sydney, Sydney, NSW 2052, Australia

²Heinz Maier-Leibniz Zentrum (MLZ) and Physik Department, Technische Universität München, D-85748 Garching, Germany

³Institut für Materialphysik im Weltraum, Deutsches Zentrum für Luft- und Raumfahrt (DLR), D-51170 Köln, Germany

⁴PETRA III, Deutsches Elektronen-Synchrotron DESY, Notkestraße 85, D-22607 Hamburg, Germany

⁵Heraeus Additive Manufacturing GmbH, Heraeusstraße 12-14, D-63405 Hanau, Germany

^{a)}Current address: Springer-Verlag GmbH, Tiergartenstraße 17, D-69121 Heidelberg, Germany.

^{b)}Author to whom correspondence should be addressed: j.kruzic@unsw.edu.au

ABSTRACT

Additive manufacturing of bulk metallic glasses (BMGs) allows for effective bypassing of critical casting thickness constraints for glassy alloys, opening up this exciting material class to new applications. An open question is how the laser processing of such materials affects the short-range structural order, a critical mediating parameter for glass deformation. Synchrotron X-ray microdiffraction was used to understand structural heterogeneity across the build-planes of a selective laser melted Zr-based BMG. While negligible macroscopic heterogeneity in the structure was observed over a 10 mm build height for the X-ray amorphous material, small periodic variations were observed on the order of 40–80 μm . This dimensional scale was rationalized as a consequence of melt-pool solidification from laser processing, which imparts a calculated local strain variation of $\pm 0.1\%$. It is anticipated that this structural insight will help to rationalize microscale deformation effects from the periodic structural variation of selective laser melting produced BMGs.

Published under license by AIP Publishing. <https://doi.org/10.1063/1.5100050>

Bulk metallic glasses (BMGs) have received considerable attention over the last few decades, largely due to their advantageous mechanical properties.^{1,2} A significant issue which has hampered their uptake as advanced engineering materials is the fast thermal transition required to maintain an amorphous state when cooling from liquid.³ If the required cooling rate is not achieved, crystallization initiates, often leading to undesirable properties. Therefore, a critical casting thickness exists for metallic glass compositions, highlighting a practical dimensional constraint relative to traditionally processed alloys.^{2,4} Additive manufacturing, and in particular, selective laser melting (SLM), has recently been found to be an effective method for overcoming such thickness constraints and to enable manufacturing of large-scale BMG components.^{3,5–7} Zr-based BMGs have been well studied in their cast form and are favorable for laser processing based on their large supercooled liquid region and thermal stability.⁸ The alloy composition $\text{Zr}_{59.3}\text{Cu}_{28.8}\text{Nb}_{1.5}\text{Al}_{10.4}$ (AMZ4) in particular has been shown to be effectively processed using SLM to form high quality BMG materials which, however, display inferior mechanical properties to its

cast counterpart.⁵ Such property differences can be related to unique structural characteristics imparted by the laser melting process,⁹ which strongly affects shear band dynamics in glasses.¹⁰ It is therefore crucial to understand the glassy structures of SLM-processed BMGs and how they are related to properties.

The mechanical properties of BMGs are tightly linked to local structural order¹¹ and structural heterogeneities,^{12,13} for both homogeneous and inhomogeneous deformation modes.¹⁴ Variations in the local clustering of atoms lead to changes in shear band dynamics and density¹⁵ and ultimately plastic deformation.^{11,16} While many open questions exist for SLM-processing BMGs, the influence of melt-pool solidification on the structural properties is perhaps the most significant. A recent study sought to investigate this for SLM-processed $\text{Zr}_{55}\text{Cu}_{30}\text{Al}_{10}\text{Ni}_5$ BMG and found that melt-pools and heat affected zones showed distinct features together with some chemical compositional variation.⁹

Here, AMZ4 powder (Heraeus GmbH, diameter 10–60 μm) was processed using an Electro Optical Systems (EOS) M290 printer with

a 400 W Yb-fiber laser and a standard EOS rotating stripe pattern with a $20\ \mu\text{m}$ layer thickness. A specimen with dimensions of $10 \times 10 \times 18\ \text{mm}^3$ was fabricated, with the longest dimension corresponding to the build direction [Fig. 1(a), inset]. A piece of the sample with the surface oriented parallel to the build direction was first polished down to $0.04\ \mu\text{m}$ surface quality (OP-S, Struers) and chemically etched using a solution of 1.5 ml hydrofluoric acid, 15 ml nitric acid, and 15 ml water (reagent grade acids) for 50 s, with post-etch neutralization in a calcium carbonate solution. The etched piece was then imaged using scanning electron microscopy (SEM, Hitachi S3400, 20 keV) with a backscattered electron detector [Fig. 1(a)] to investigate variation in relative density. Etching occurred preferentially at melt-pool boundaries, allowing for observation of the thermally induced patterns in the AMZ4 structure.⁹ The thickness of the complex melt-pool pattern was approximately $60\ \mu\text{m}$ [white dashed lines, Fig. 1(a)]. To investigate the effect of the structure on the mechanical properties, the same piece was again ground and polished and investigated using nanoindentation with a diamond Berkovich probe (Hysitron TI 950, Bruker). A 2D map with dimensions of $200 \times 30\ \mu\text{m}^2$ (21×4 indents, $10\ \mu\text{m}$ indent spacing) is shown in Fig. 1(b), indicating a higher reduced elastic modulus (E_R) in regions which could be rationalized as melt-pool boundaries, when considering the spatial correlation between nanoindentation mapping and the thermal patterns observed in Fig. 1(a). Indeed, recent investigations have drawn links between the local atomic structure and the elastic properties in BMGs, also determined using nanoindentation.¹⁷

As seen in Fig. 1, thermal processing from SLM leads to a variation in the structure and mechanical properties along the build height. Such a variation could be a result of elemental segregation, partial crystallization, or oxidation at the melt-pool boundaries. Energy-dispersive X-ray spectroscopy was performed over the sample cross section; however, no elemental segregation correlating with melt-pool spacing was observed, suggesting that significant compositional variability does not exist between melt-pools and heat affected zones. To understand these melt-pool solidification effects in more detail, the glass was

investigated using high energy synchrotron X-ray microdiffraction. Relative to other techniques, such as transmission electron microscopy, synchrotron X-ray microdiffraction enables the investigation of short- and medium-range ordering (SRO and MRO) of amorphous structures over large areas to include the entire build height while also resolving the microscale of the structural variations observed in Fig. 1. This technique is well established for investigating structural evolution^{18–20} and strains in BMGs.^{21–25}

For the synchrotron measurements, thin strips ($\sim 1.5 \times 18 \times 0.15\ \text{mm}^3$) were cut from both the “center” and “edge” of the AMZ4 block with a low speed diamond saw (Buehler IsoMet) and the surface was ground with 4000 grit SiC paper to remove surface asperities. Samples were cleaned with acetone and ethanol and then adhered to an Al window (vacuum-grade Al, wire electrical discharge machined) for the X-ray measurements. Measurements were performed in the 2nd experimental hutch of the PETRA III P07 beamline at the Deutsches Elektronen-Synchrotron (DESY) in Hamburg, Germany. Spatially resolved X-ray diffraction line-scans were performed from the bottom of the sample using a microfocussed monochromatic photon beam with an energy of 98.15 keV and a size of $30 \times 2\ \mu\text{m}^2$ ($w \times h$) attained using an Al compound refractive lens system. The resultant X-ray scattering patterns were collected on a PILATUS3 X CdTe 2M detector with an exposure time of 2 s used for all tests and showed a fully amorphous structure absent of any intermetallic crystallites or oxides. A $2\ \mu\text{m}$ step-size along the z -axis was used along the sample build-length ($z = 9.8\ \text{mm}$) correlating with approximately 4900 diffraction images per sample. The collected 2D diffraction patterns were integrated over the full azimuthal range using the Python pyFAI package.²⁶ Measured data $I_m(Q)$ were then processed using PDFgetX3,²⁷ to allow for the determination of the structure function $S(Q)$ [Fig. 2(a)],

$$S(Q) = \frac{I_c(Q) - \langle f(Q)^2 \rangle + \langle f(Q) \rangle^2}{\langle f(Q) \rangle^2} \quad \text{with}$$

$$I_m(Q) = a(Q)I_c(Q) + b(Q), \quad (1)$$

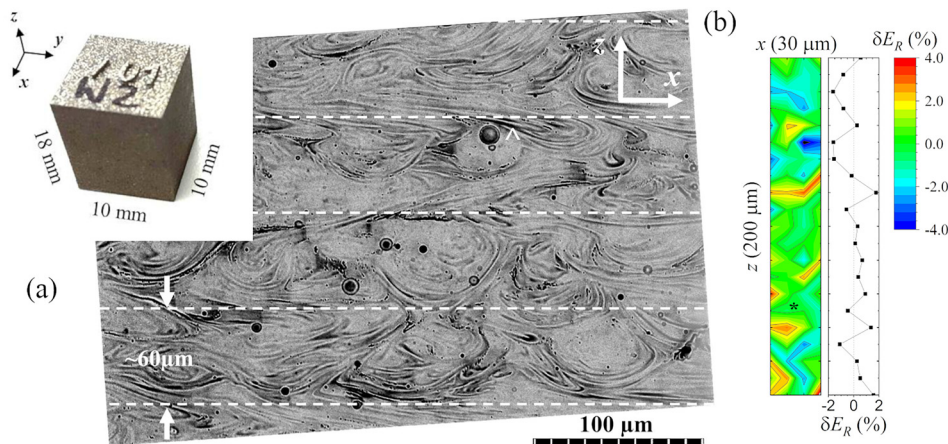


FIG. 1. Backscattered electron micrograph of the chemically etched cross section shows melt-pool layers with an approximate height of $60\ \mu\text{m}$ (a). The “inset” contains a photograph of the SLM-processed AMZ4 block from which all samples were cut (z -direction equivalent to the build direction). Nanoindentation mapping and line-scan average of the cross section highlight reduced modulus variation δE_R along the cross section [(b), the same scale as the micrograph]. NB: Smaller particles in the micrograph are likely precipitates from chemical etching; the spherical particle (marked *) is an unmelted AMZ4 particle defect; one poor quality indent (marked *) in the nanoindentation map was replaced with the mean E_R value.

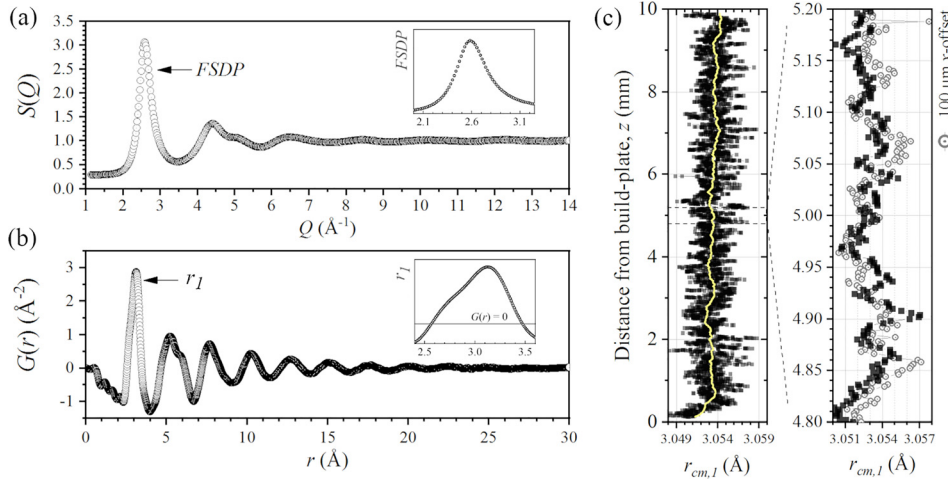


FIG. 2. Representative $S(Q)$ and $G(r)$ data from the X-ray measurement [(a) and (b), respectively]. Insets provide an enhancement of the FSDP and r_1 . The first significant peak mass-center for $G(r)$ $r_{cm,1}$ shows a negligible change in the average peak-center along the build height (highlighted by 150 pt. moving average, yellow line) but a distinct periodic variation (c), while scanning with a $100\ \mu\text{m}$ offset in the x -direction provides $r_{cm,1}$ distributions which overlay closely with the original data.

where $I_c(Q)$ is the coherent scattering intensity, determined from the measured intensity I_m from the total scattering experiment and multiplicative $a(Q)$ and additive $b(Q)$ corrections. Examples for effects corrected by $a(Q)$ are the sample absorption and X-ray polarization, while $b(Q)$ corrects for Compton scattering and any background scattering from the sample container or environment. Additionally, $f(Q)$ is the atomic scattering factor, and angle brackets indicate an average over all atom types in the sample (Zr, Cu, Al, and Nb). The $S(Q)$ was then Fourier transformed to obtain the reduced pair distribution function (PDF), $G(r)$ [Fig. 2(b)],

$$G(r) = \frac{2}{\pi} \int_{Q_{\min}}^{Q_{\max}} Q[S(Q) - 1] \sin Qr dQ, \quad (2)$$

integrated between Q_{\min} 0.7 and Q_{\max} $14\ \text{\AA}^{-1}$. For the quaternary glass studied, the peak position is the most robust structural feature, especially when considering likely thickness variation along the sample height. Peaks in the $S(Q)$ data were fit with a pseudo-Voigt function between $2.45 \leq Q \leq 2.9\ \text{\AA}^{-1}$. For $G(r)$, the peak center-of-mass r_{cm} was determined using

$$r_{cm} = \frac{\int_{r_{\min}}^{r_{\max}} rG(r)}{\int_{r_{\min}}^{r_{\max}} G(r)}, \quad (3)$$

where r_{\max} and r_{\min} are the intersection coordinates of $G(r)$ with the line $G(r) = 0$.

When plotting the r_{cm} of the first significant peak in $G(r)$, $r_{cm,1}$, against the build-height for the center sample, a periodic variation in the interatomic distance was seen with no observable change in the moving average over 10 mm of build height [Fig. 2(c)]. Some variation was observed toward the ends of the scan height ($z \rightarrow 0, 10\ \text{mm}$), but this was likely caused by X-ray interference with the sample holder. From 0.5 to 9.5 mm of build-height, a moving point average shows negligible deviation from $3.053 \pm 0.002\ \text{\AA}$, although a significant periodic $r_{cm,1}$ variation exists between 3.050 and 3.057 \AA . While the magnitude of these changes is small, they correspond well to the work of Wei *et al.* for the AMZ4 structural variation during thermal relaxation.¹⁸ Using a custom Python code, average distances between maxima for Savitzky-Golay filtered (window length 19, polynomial

order 3) $r_{cm,1}$ data as a function of build-height were determined as $58 \pm 23\ \mu\text{m}$, correlating well with the melt-layer thickness of $\sim 60\ \mu\text{m}$ observed in Fig. 1(a). The measurement was additionally performed with x -axis offsets of $100\ \mu\text{m}$ and $200\ \mu\text{m}$, and when considering the same z range, peak maxima occur at comparable positions [for $100\ \mu\text{m}$ offset data, see Fig. 2(c)]. An average maxima spacing of $58 \pm 22\ \mu\text{m}$ was determined for both $100\ \mu\text{m}$ and $200\ \mu\text{m}$ offsets, correlating well with the initial scan, and infers a physical link to the melt-pool solidification results highlighted in Fig. 1. Measurements performed on a sample taken from the edge of the printed block have an identical r_{cm} magnitude ($3.053 \pm 0.001\ \text{\AA}$); however, they show an average maxima spacing of $64 \pm 25\ \mu\text{m}$ which do not align with the maxima positions of Fig. 2(c). Negligible differences in $r_{cm,1}$ exist between the edge and center of the printed BMG block, which suggests a broadly homogeneous average glass structure throughout the whole block. While commensurate shifts were also observed in $G(r)$ for peaks $> r_1$, peak broadening in higher Q -ranges leads to poorer resolved PDF data, and as such, only r_1 is studied in more detail.

While the $r_{cm,1}$ variation in $G(r)$ can be connected spatially to metallography and nanoindentation results (Fig. 1), it is noted that data analysis artifacts or residual stresses in the material may also be responsible for shifts in $r_{cm,1}$. To confirm that the $r_{cm,1}$ shifts were due to structure variation, data points corresponding to minima (A), neutral (B), and maxima (C) for a period of large $G(r)$ fluctuations were investigated in more detail (Fig. 3). From the individual diffraction patterns, shifts are seen in the $S(Q)$ first sharp diffraction peak (FSDP) fit with a pseudo-Voigt function, further lending to the view that $G(r)$ variations have physical origins and indicating that the Fourier transformation of $S(Q)$ does not impart some artificial variability into the $G(r)$ result.

When taking an azimuthal integration range of 30° for $I(Q)$, only a very slight variation is seen as a function of azimuthal angle (φ), i.e., small elliptical distortions of the diffraction pattern [Figs. 3(c) and 3(d)]. Elliptical distortions of the diffraction rings in amorphous materials have been reasoned to be due to the presence of local strain fields,²⁸ as for shot-peened surface layers.²⁹ The small distortions suggest that residual stresses from laser processing are near-negligible in the samples studied and indicates that variations in the $S(Q)$ FSDP

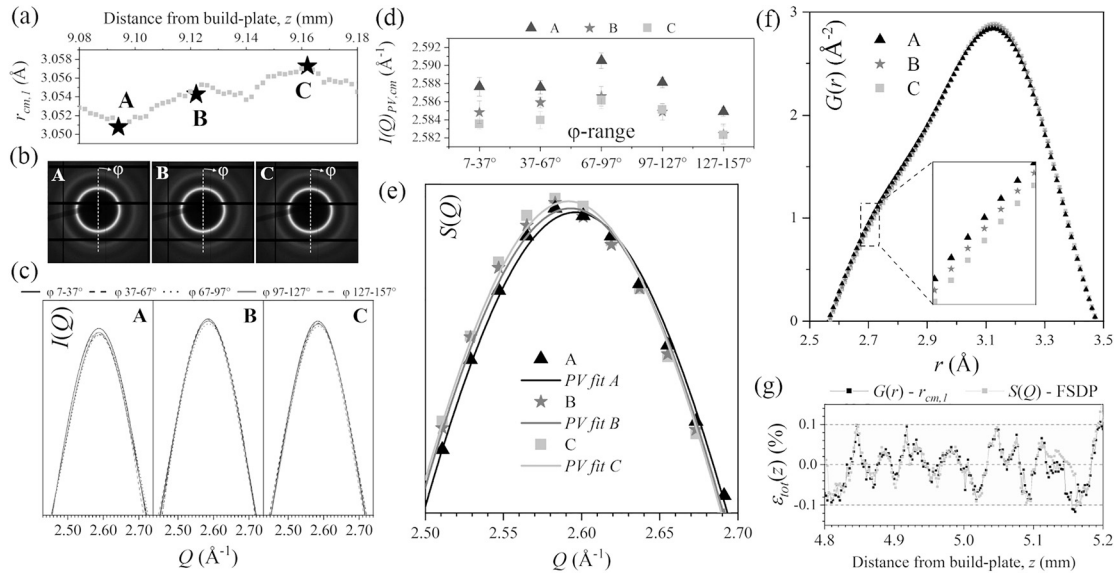


FIG. 3. Comparing the extremes of the $r_{cm,1}$ variation (a) derived from the collected diffraction patterns (b) show subtle variance in the $G(r)$ r_1 and $S(Q)$ FSDP [(e) and (f)]. Azimuthal integration of the diffraction rings over 30° increments shows slight elliptical distortion of the diffraction pattern (c), as noted for the change in fitted pseudo-Voigt (PV) mass-center for the intensity FSDP ($I(Q)_{PV,cm}$) as a function of azimuthal angle (d). The small peak intensity changes in $I(Q)$ of $\sim 1.5\%$ are within the pixel gain homogeneity limits. Also shown is the local strain $\varepsilon_{tot}(z)$ calculated using both $G(r)$ $r_{cm,1}$ and $S(Q)$ FSDP data (g).

and $r_{cm,1}$ are dominated by structural variations in the metallic glass along the build-height.

Based on the method developed by Poulsen²⁸ and further outlined by Shakur Shahabi *et al.*,^{23,24} it is possible to estimate the local strain from the variations in the $G(r)$ peak position observed in Fig. 2(c), using

$$\varepsilon(z) = \frac{r_{cm}(z) - r_{cm}^0(z)}{r_{cm}^0(z)}, \quad (4)$$

where the reference position $r_{cm}^0(z)$ is hereby determined as the sample position in which filtered $r_{cm}(z)$ data (Savitzky-Golay, window length 31 and polynomial order 3) have a derivative of zero or

$$r_{cm}^0(z) = r_{cm}(z) \Big|_{dr_{cm}/dz=0}. \quad (5)$$

The value $r_{cm}^0(z)$ oscillates between local maxima and minima. If the displacements with respect to the reference points next to $r_{cm}^0(z)^+$, and previous to $r_{cm}^0(z)^-$, are assumed to contribute equally to the total strain at z , then the total strain can be written as

$$\varepsilon_{tot}(z) = \frac{[\varepsilon(z)^+ + \varepsilon(z)^-]}{2} = \frac{1}{2} \left[\frac{r_{cm}(z) - r_{cm}^0(z)^+}{r_{cm}^0(z)^+} + \frac{r_{cm}(z) - r_{cm}^0(z)^-}{r_{cm}^0(z)^-} \right]. \quad (6)$$

Similarly, the total strain can be calculated using the data in reciprocal space [i.e., from $S(Q)$]. From both real- and reciprocal-space analyses, a variation in local strain of $\pm 0.1\%$ (or local stresses of ± 85 MPa based on the reported elastic modulus³⁰) was determined along the build-height

[Fig. 3(g)], comparable to a report on the strain measured over single shear bands in cold-rolled Vit105 BMG.²⁴ In contrast, *in situ* mechanical compression measurements show strains on the order of 1.0%–2.0%.²³ These local strains are inherently linked to structural density within, and between, shear transformation zones. However, it is also important to note that the diffraction pattern is recorded over the entire interaction volume ($2 \times 30 \times 150 \mu\text{m}^3$), and actual local variations may indeed be more pronounced than the magnitudes reported here.

Shifts in the $S(Q)$ FSDP can be related to variations in the local fictive temperature, free volume, and structural relaxation state in the glass. Similar conclusions have been drawn for glassy $\text{Pd}_{40}\text{Cu}_{30}\text{Ni}_{10}\text{P}_{20}$ ribbons studied using high energy photons³¹ and for thermally cycled La-based BMGs.³² While for multicomponent glasses, the $S(Q)$ FSDP is related to a number of complex factors,³³ Ma *et al.* have also related shifting of this peak to variability in the MRO.³⁴ This supports broad observations of shifts occurring in $G(r)$ for peaks $> r_1$ corresponding to MRO. Such observed structural periodicity over the short- and medium-range length scales correlates well with the results of Fig. 1, which highlights a spatial variation in local density as a result of the thermal history. As such, maxima in the $r_{cm,1}$ variation link to a shift in the $S(Q)$ FSDP to lower Q values which may be caused by higher cooling rates at the melt-pool boundaries leading to thermal gradients. Moreover, the small changes in $r_{cm,1}$ are a result of variations in the partial PDFs for selected atomic pairs. For $\text{Zr}_{60}\text{Cu}_{30}\text{Al}_{10}$, Tong *et al.* determined the partial PDFs from molecular dynamics simulations,³⁵ where in Fig. 3(f), the left shoulder in $G(r)$ corresponds to Zr-Cu pairs and the main peak to Zr-Zr pairs. Such an observation may indicate a small chemical SRO variation together with the variation of the inter-atomic distances during structural relaxation, consistent with recently reported results regarding the variation of Zr/Cu between heat affected zones and melt-pools.⁹

The origin of this reported structural variation is likely a result of melt-pool solidification dynamics during SLM-processing, which imbues structural changes dependent on the local cooling rate.³ These solidification processes have recently been shown to have a significant effect on the local BMG structure, between molten pools and heat affected zones,⁹ and it is clear here that this manifests as a structural variation over short- and medium-range length scales with consequent effects on the local mechanical properties. It is promising, however, that the SLM-processed AMZ4 retains a bulk X-ray amorphous structure throughout the build despite the apparent periodic variations in the cooling rate. The influence of this microscale periodic variation on the bulk mechanical properties will be the focus of further work in this area.

We acknowledge DESY (Hamburg, Germany), a member of the Helmholtz Association HGF, for the provision of experimental facilities. Parts of this research were carried out at PETRA III at the P07 beamline. We also acknowledge the Deutscher Akademischer Austauschdienst (DAAD) through the Australia-Germany Joint Research Co-operation Scheme (UA-DAAD, Nos. 57386795 and 57447466) for funding and staff at the Australian National Fabrication Facility (ANFF) for their support in chemical etching. J. J. Kruzic also acknowledges financial support from Australian Research Council Discovery Grant No. DP180101393. This research used the facilities at the Electron Microscope Unit and Solid State and Elemental Analysis Unit at UNSW. The authors also thank Matthias Kolbe of DLR for performing the energy-dispersive X-ray spectroscopy analysis.

REFERENCES

- ¹J. J. Kruzic, *Adv. Eng. Mater.* **18**, 1308 (2016).
- ²A. L. Greer, *Mater. Today* **12**, 14 (2009).
- ³S. Pauly, L. Löber, R. Petters, M. Stoica, S. Scudino, U. Kühn, and J. Eckert, *Mater. Today* **16**, 37 (2013).
- ⁴A. Inoue, *Acta Mater.* **48**, 279 (2000).
- ⁵P. Bordeenithikasem, M. Stolpe, A. Elsen, and D. C. Hofmann, *Addit. Manuf.* **21**, 312 (2018).
- ⁶D. Ouyang, N. Li, W. Xing, J. Zhang, and L. Liu, *Intermetallics* **90**, 128 (2017).
- ⁷X. P. Li, M. P. Roberts, S. O'Keefe, and T. B. Sercombe, *Mater. Des.* **112**, 217 (2016).
- ⁸A. Inoue, T. Zhang, N. Nishiyama, K. Ohba, and T. Masumoto, *Mater. Trans. JIM* **34**, 1234 (1993).
- ⁹D. Ouyang, N. Li, and L. Liu, *J. Alloys Compd.* **740**, 603 (2018).
- ¹⁰P. Zhao, J. Li, J. Hwang, and Y. Wang, *Acta Mater.* **134**, 104 (2017).
- ¹¹A. L. Greer, Y. Q. Cheng, and E. Ma, *Mater. Sci. Eng. R* **74**, 71 (2013).
- ¹²B. A. Sun and W. H. Wang, *Prog. Mater. Sci.* **74**, 211 (2015).
- ¹³C. A. Schuh, T. C. Hufnagel, and U. Ramamurty, *Acta Mater.* **55**, 4067 (2007).
- ¹⁴C. Suryanarayana and A. Inoue, *Bulk Metallic Glasses* (CRC Press, 2010).
- ¹⁵Z.-Y. Yang, Y.-J. Wang, and L.-H. Dai, *Scr. Mater.* **162**, 141 (2019).
- ¹⁶A. S. Argon, *Acta Metall.* **27**, 47 (1979).
- ¹⁷C. Ebner, B. Escher, C. Gammer, J. Eckert, S. Pauly, and C. Rentenberger, *Acta Mater.* **160**, 147 (2018).
- ¹⁸S. Wei, M. Stolpe, O. Gross, Z. Evenson, I. Gallino, W. Hembree, J. Bednarcik, J. J. Kruzic, and R. Busch, *Appl. Phys. Lett.* **106**, 181901 (2015).
- ¹⁹Z. Evenson, S. E. Naleway, S. Wei, O. Gross, J. J. Kruzic, I. Gallino, W. Possart, M. Stommel, and R. Busch, *Phys. Rev. B* **89**, 174204 (2014).
- ²⁰W. Dmowski, Y. Yokoyama, A. Chuang, Y. Ren, M. Umemoto, K. Tsuchiya, A. Inoue, and T. Egami, *Acta Mater.* **58**, 429 (2010).
- ²¹J. Gamcová, G. Mohanty, Š. Michalík, J. Wehrs, J. Bednarčík, C. Krywka, J. M. Breguet, J. Michler, and H. Franz, *Appl. Phys. Lett.* **108**, 031907 (2016).
- ²²T. C. Hufnagel, U. K. Vempati, and J. D. Almer, *PLoS One* **8**, e83289 (2013).
- ²³H. Shakur Shahabi, S. Scudino, I. Kaban, M. Stoica, U. Rütt, U. Kühn, and J. Eckert, *Acta Mater.* **95**, 30 (2015).
- ²⁴H. Shakur Shahabi, S. Scudino, I. Kaban, M. Stoica, B. Escher, S. Menzel, G. B. M. Vaughan, U. Kühn, and J. Eckert, *Acta Mater.* **111**, 187 (2016).
- ²⁵S. Scudino, R. N. Shahid, B. Escher, M. Stoica, B. S. Li, and J. J. Kruzic, *Appl. Phys. Lett.* **110**, 081903 (2017).
- ²⁶J. Kieffer and D. Karkoulis, *J. Phys. Conf. Ser.* **425**, 202012 (2013).
- ²⁷P. Juhás, T. Davis, C. L. Farrow, and S. J. L. Billinge, *J. Appl. Crystallogr.* **46**, 560 (2013).
- ²⁸H. F. Poulsen, J. A. Wert, J. Neufeind, V. Honkimäki, and M. Daymond, *Nat. Mater.* **4**, 33 (2005).
- ²⁹F. O. Mear, G. Vaughan, A. R. Yavari, and A. L. Greer, *Philos. Mag. Lett.* **88**, 757 (2008).
- ³⁰Heraeus Datasheet, *Metal Powder AMZA (ZrCuAlNb)* (Heraeus Additive Manufacturing GmbH, Hanau, Germany, 2018).
- ³¹A. R. Yavari, A. Le Moulec, A. Inoue, N. Nishiyama, N. Lupu, E. Matsubara, W. J. Botta, G. Vaughan, M. Di Michiel, and Å. Kvick, *Acta Mater.* **53**, 1611 (2005).
- ³²J. Bednarcik, S. Michalík, M. Sikorski, C. Curfs, X. D. Wang, J. Z. Jiang, and H. Franz, *J. Phys. Condens. Matter* **23**, 254204 (2011).
- ³³N. Mattern, *Appl. Phys. Lett.* **105**, 256101 (2014).
- ³⁴D. Ma, A. D. Stoica, and X. L. Wang, *Nat. Mater.* **8**, 30 (2009).
- ³⁵P. Tong, D. Louca, G. Wang, P. K. Liaw, Y. Yokoyama, A. Llobet, H. Kawaji, Y. Qiu, and Y. Shi, *Metals (Basel)* **2**, 529 (2012).